SmartMat

WILEY

SmartMat Open Access

RESEARCH ARTICLE OPEN ACCESS

Sputtered Ultra-Thin TiO_2 Interlayer for Highly Reversible Aqueous Zinc-Ion Battery

Qiuxia Zhang[1] | Linfeng Wan[1] | Shaoheng Cheng[1] | Jiantao Wang[2] | Yuhang Dai[3] | Xuan Gao[4] | Guanjie He[4] | Hongdong Li[1]

[1]State Key Laboratory of High Pressure and Superhard Materials, College of Physics, Jilin University, Changchun, China | [2]State Key Laboratory of Powder Metallurgy, Central South University, Changsha, China | [3]Department of Engineering Science, University of Oxford, Oxford, UK | [4]Christopher Ingold Laboratory, Department of Chemistry, University College London, London, UK

Correspondence: Jiantao Wang (wangjiantaocsu@163.com) | Yuhang Dai (yuhang.dai@eng.ox.ac.uk) | Xuan Gao (xuan.gao.21@ucl.ac.uk) | Guanjie He (g.he@ucl.ac.uk) | Hongdong Li (hdli@jlu.edu.cn)

Received: 29 April 2025 | **Revised:** 21 June 2025 | **Accepted:** 30 June 2025

Funding: This work was supported by the National Natural Science Foundation of China (52172044), the Engineering and Physical Sciences Research Council (EP/V027433/1), and the Physical Sciences Research Council (EP/V027433/2).

Keywords: aqueous zinc-ion batteries | artificial interlayer | physical barrier | Zn anode interface

ABSTRACT

Undesirable side reactions at the Zn anode interface hindered the development of aqueous zinc-ion batteries (AZIBs). In particular, the direct contact between the zinc (Zn) anode and aqueous media triggers side reactions such as Zn dendrites, hydrogen evolution, and corrosion. In this study, an artificial interlayer (TiO_2) is constructed on the Zn anode surface by magnetron sputtering technology. Thanks to its ultra-thin, uniform, and stable porous structure, the TiO_2 interlayer can effectively suppress and reduce side reactions through a physical barrier and regulation of ion flux. The experimental results show that the Zn||Zn symmetric cells using Zn anode with TiO_2 interlayer (TO-Zn) exhibit symmetric charge–discharge curves and an ultra-long cycle life of over 5100 h at 5 mA/cm^2 (1 mA•h/cm^2), which is approximately 51 times longer than the bare Zn anode (only 100 h). Compared to the bare Zn||MnO_2 full cell, the full cell assembled with TO-Zn exhibits a relatively stable cycling performance, retaining a reversible capacity of approximately 108.4 mA•h/g after 1000 cycles. This study uses a facile process technology to provide a reference for constructing an artificial interlayer.

1 | Introduction

Compared with traditional lithium-ion and lead-acid batteries, aqueous zinc-ion batteries (AZIBs) offer the benefits of safety and sustainability, abundant zinc (Zn) resources, and low preparation costs [1, 2]. Particularly, the Zn metal can provide a suitable redox potential (−0.76 V vs. standard hydrogen electrodes) and a substantial theoretical capacity (820 mA•h/g) [3]. Therefore, AZIBs have enormous potential market applications. Due to the thermodynamic instability of metallic Zn and the nonuniform deposition of Zn^{2+}, Zn dendrites form on the anode surface. These dendrites can penetrate the separator, causing internal short circuits. Moreover, the Zn dendritic morphology increases local current density, accelerates parasitic reactions (e.g., hydrogen evolution reactions [HERs] and corrosion), and intensifies the formation of inactive "dead zinc." These issues severely affect the battery's cycling stability, coulombic efficiency (CE), and capacity, seriously hindering the further development of AZIBs [4].

Researchers have devised many strategies to mitigate these parasitic reactions and enhance battery cycling stability, including electrolyte additives [5], surface modification [6], and artificial interlayers [7, 8]. The construction of artificial interlayers serves as an effective protective barrier between Zn anodes and aqueous electrolytes. First, by

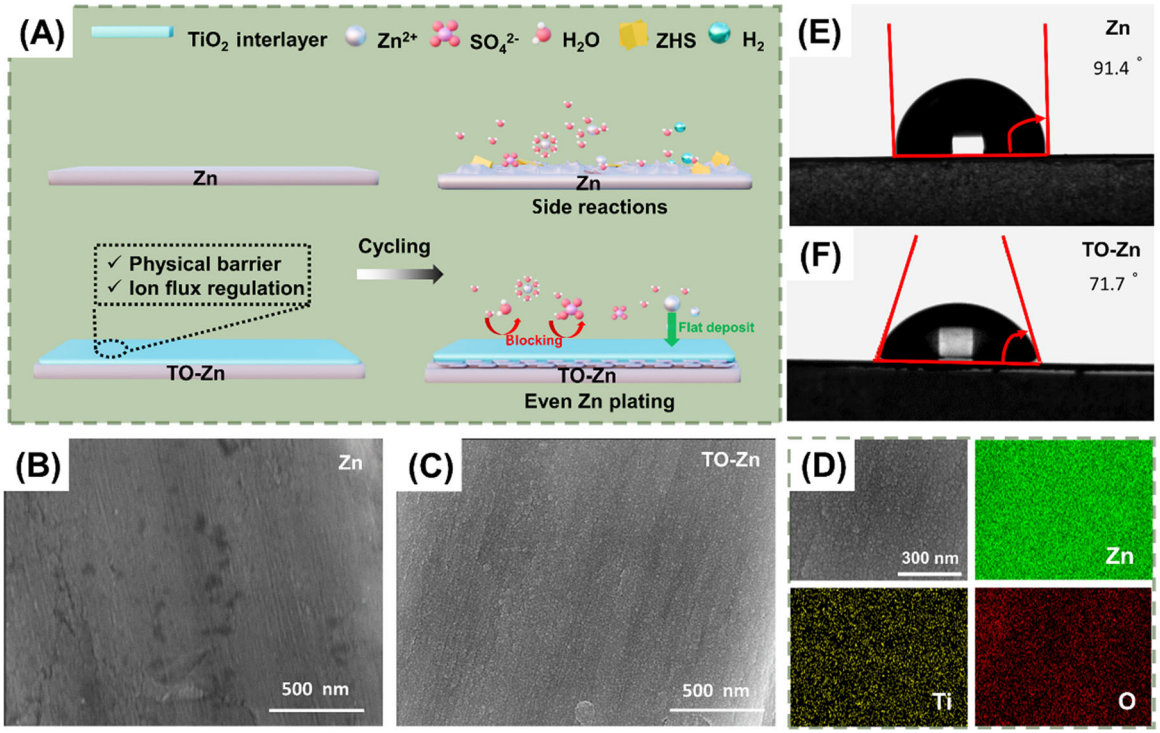

FIGURE 1 | (A) Schematic diagram of Zn^{2+} deposition mechanism using the bare Zn and TO-Zn anodes. SEM images of (B) bare Zn anode and (C) TO-Zn anode. (D) SEM image and EDS of the TO-Zn anode. Contact angle measurements of (E) bare Zn anode and (F) TO-Zn anode with zinc sulfate electrolyte (2 mol/L $ZnSO_4$).

avoiding the Zn anode from direct contact with aqueous electrolytes, the artificial interlayer can suppress the HER and corrosion. Second, the artificial interlayer has the tunability of physicochemical characteristics, which can homogenize Zn^{2+} flux, induce uniform Zn plating/stripping, avoid the Zn dendrite formation, and improve cycling stability. According to the preparation methods, the strategies for constructing artificial interlayers can be categorized based on preparation methodology into in situ and ex situ synthesis. Ex situ synthesis approaches mainly involve doctor blade coating and spin-coating [9, 10]. For example, Wang et al. [11] synthesized WSe_2/ZIF composite materials using a multistep hydrothermal method, then used as the interlayer by a spin-coating method. There are many types of in situ techniques, such as physical/chemical vapor deposition (PVD/CVD), atomic/molecular layer deposition (ALD/MLD), liquid phase deposition (LPD), etc. [12–15]. Hao et al. [14] used a high-temperature vapor–solid method to introduce a uniformly dense ZnS artificial protective interlayer, achieving a Zn anode without side reactions. Liu et al. [15] constructed an ultra-thin ZrO_2 interlayer by ALD on Zn anodes, establishing both physical protection and controlled interface polarization. Zhang et al. [13] in situ constructed an artificial interlayer ($Zn_3(PO_4)_2{\cdot}4H_2O$) on Zn foil by the hydrothermal method to inhibit the Zn dendrite growth.

However, the above artificial interlayer typically has the following drawbacks: poor repeatability, over-thickness, non-uniformity, and weak adhesion, which result in slow reaction kinetics, uneven deposition, and poor Zn anode interface stability. Additionally, it must consider the toxicity of materials, cost, and complexity of processes [16]. Therefore, it is essential to find an efficient preparation process and eco-friendly materials. Magnetron sputtering is a widely used and versatile surface coating technology, and it has been used in electronic devices, optical components, biomedical, and other fields [17–21]. Compared with the above methods of constructing artificial interlayer, magnetron sputtering has the advantages of good uniformity, strong adhesion, and high cost-effectiveness [22]. This work prepared an ultra-thin artificial interlayer of titanium oxide (TiO_2) on the Zn anode surface by magnetron sputtering. Firstly, TiO_2 has good chemical inertness and structural stability, which can act as a physical barrier to prevent direct contact between the Zn anode and H_2O, thereby inhibiting corrosion and HER [23]. Second, the TiO_2 interlayer has a rough surface and a uniform nanoscale pore, which can regulate ion flux and limit two-dimensional (2D) diffusion processes, guiding the Zn^{2+} uniform deposition [24]. In addition, the TiO_2 interlayer (metal oxide semiconductor thin film) can eliminate the "tip effect" and inhibit the growth of Zn dendrites by the electrostatic shielding effect [25]. Combining the advantages of a simple process, good film quality of sputtering technology, and the TiO_2's excellent properties. The TO-Zn exhibited consistent charge–discharge curves in the assembled Zn||Zn symmetric cells without significant fluctuations, achieving an ultra-long cycle life of over 5100 h. The Zn||MnO_2 full cells assembled using TO-Zn (with a mass load of approximately 3.8 mg/cm^2) have a higher specific capacity (108.4 mA•h/g) over 1000 cycles.

2 | Result and Discussion

As shown in Figure 1A, a TiO_2 interlayer was deposited on the Zn anode surface by the magnetron sputtering technique [22]. Specifically, when subjected to high-energy particle

bombardment, the Ti target material was evaporated into the gaseous phase, and Ti atoms in the gas phase were subsequently deposited on the Zn anode surface. During this process, due to sufficient oxygen in the magnetron cavity, Ti in an atomic state is prone to form TiO_2. The TiO_2 interlayer can serve as a barrier against H_2O and SO_4^{2-}, preventing the Zn anode from direct contact with the electrolyte, thereby mitigating corrosion and HER [23]. In addition, the uniform nanoscale pore of the interlayer can homogenize Zn^{2+} flow and promote the Zn^{2+} uniform deposition [24].

The bare Zn and TO-Zn surface morphology before cycling was characterized by scanning electron microscopy (SEM), as shown in Figures 1B,C and S1. In comparison to the bare Zn anode, the TO-Zn anode surface exhibits uniform nanoscale pores without prominent clusters. As shown in Figure 1D, energy dispersive spectroscopy (EDS) analysis of the TO-Zn anode surface reveals a uniform distribution of Ti and O elements, and further confirms that the artificial interlayer constructed by the sputtering technique has high uniformity. The wettability of the artificial interlayer is critical to the Zn^{2+} deposition behavior by affecting the electrolyte wettability at the Zn anode surface. Figure 1E,F shows that the tested contact angle of TO-Zn (71.7°) is less than that of bare Zn (90.5°). A smaller contact angle enables a more hydrophilic surface, facilitating electrolyte wetting, effectively reducing interface impedance, and improving reaction kinetics [26, 27].

The structure of the TiO_2 interlayer was analyzed by X-ray diffraction (XRD) (Figure 2A). The XRD spectroscopy shows strong peaks at 36.2° and 43.2°, corresponding to the Zn (002) and Zn (101) crystal planes, respectively [28]. There is no evident diffraction peak of TiO_2, which is due to the insufficient content of TiO_2 on the Zn surface not meeting the detection requirements. Therefore, the chemical identity and bonding states of the TiO_2 interlayer were analyzed using X-ray photoelectron spectroscopy (XPS). As shown in Figure 2B, the orbital-resolved XPS spectrum of Ti displays the Ti^{4+} $2p_{3/2}$ with a binding energy of 458.5 eV and the Ti^{4+} $2p_{1/2}$ with a binding energy of 464.1 eV, which belong to Ti–O bonds and are characteristic of the TiO_2 crystal structure [29]. In Figure 2C, the three peaks at 530.0, 531.9, and 532.9 eV may correspond to the lattice oxygen, oxygen vacancies, and surface-adsorbed oxygen of TiO_2, respectively [30]. The peak of oxygen vacancies at 531.9 eV is strong, indicating that the TiO_2 interlayer has rich oxygen vacancies, which can promote rapid Zn^{2+} transfer [31]. The binding energies between Zn atoms on bare Zn and TO-Zn anodes were computationally determined through density functional theory (DFT), as shown in Figure S2. The calculations reveal that the Zn atom binding energies of −0.81 eV

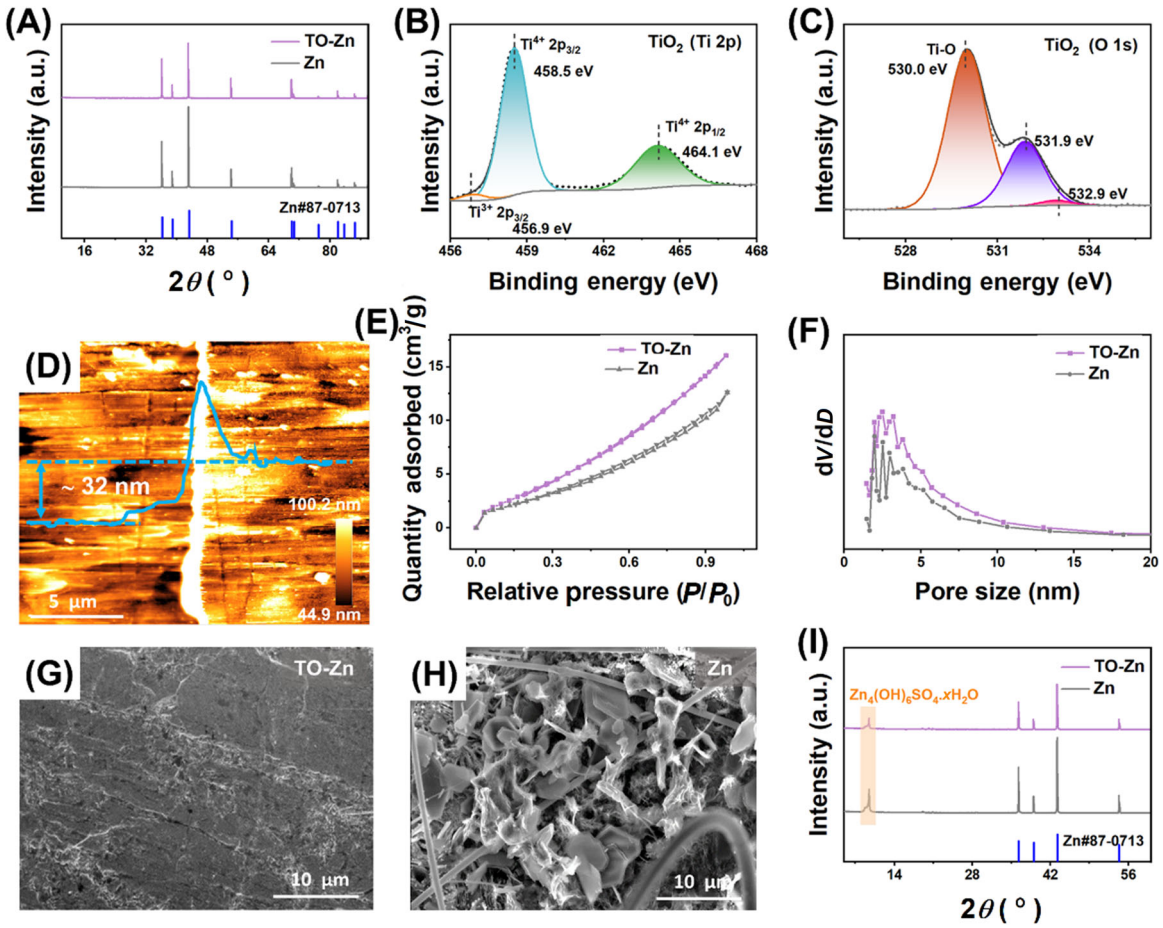

FIGURE 2 | (A) XRD patterns of the bare Zn and TO-Zn anodes. XPS spectra survey of (B) Ti 2p and (C) O 1s peaks for the TiO_2 interlayer. (D) The AFM image was taken at the step edge of the TiO_2 interlayer on a Zn anode surface. (E) Surface porosity characteristics from N_2 adsorption–desorption measurements and (F) corresponding pore size distributions of the bare Zn and TO-Zn anodes. (G, H) The SEM images and corresponding (I) XRD patterns of the bare Zn and TO-Zn surface resulted from the Zn||Zn symmetric cells after 10 cycles at 1 mA/cm^2 (1 mA•h/cm^2).

(bare Zn anode) versus −0.45 eV (TO-Zn anode). The binding energy of Zn atoms on the TiO_2 interlayer is weaker, indicating that the TiO_2 interlayer can make Zn^{2+} more quickly pass through the surface, significantly suppressing Zn dendrite formation while improving the interfacial stability of Zn anodes [23, 31].

As shown in Figure 2D, the thickness of the TiO_2 interlayer on the Zn surface is about 32 nm by atomic force microscopy (AFM). The typical Type IV isothermal adsorption–desorption curve is measured by the BET method. After sputtering the TiO_2 interlayer on the Zn surface, the BET multipoint specific surface area significantly increased from 10.8 m^2/g (Zn) to 15.6 m^2/g (TO-Zn), and the pore size of the TiO_2 interlayer is approximately 5 nm (Figure 2E,F). The nanoscale pore is beneficial for homogenizing Zn^{2+} flux and promoting uniform Zn^{2+} deposition [29]. In addition, AFM also showed that the roughness of the bare Zn surface was 7.38 nm, while the TiO_2 interlayer was 8.45 nm (Figure S3). The results correlate well with the BET surface area measurements, indicating that the surface of the TiO_2 interlayer is rougher, which is conducive to homogenizing ion flux and Zn^{2+} deposition behavior.

The bare Zn and TO-Zn surface morphology of Zn||Zn symmetric cells after cycling was preliminarily characterized by SEM. As shown in Figure 2G,H, after 10 cycles at 1 mA/cm^2 (1 mA•h/cm^2), the TO-Zn surface retains remarkable surface uniformity, indicating that the TiO_2 interlayer (metal oxide semiconductor thin film) can utilize electrostatic shielding to eliminate the "tip effect" and achieve smooth-morphology Zn anode [32]. In contrast, many rough and anisotropic Zn dendrites appeared on the bare Zn surface, and EDS results showed significant by-product formation (Figure S4) [33]. As shown in Figure 2I, the XRD patterns further confirm the by-products ($Zn_4(OH)_6SO_4{\cdot}xH_2O$, ZHS) on the bare Zn. Under high-current operation (after one cycle at 10 mA/cm^2 (10 mA•h/cm^2)), the Zn dendrites phenomenon is more obvious, as shown in Figure S5. The Zn^{2+} deposition behavior on the bare Zn surface is mainly Zn (101), which promotes the crazy growth of Zn dendrites. The deposition behavior on the TO-Zn surface is mainly Zn (002), which helps achieve even surface deposition [34].

The exchange current density is associated with the Zn^{2+} deposition process at different current densities (Figure S6), representing the electrode's redox reaction rate under equilibrium potential, as calculated from Equation (1) [35].

$$i = i_0 \frac{F}{RT}\left(\frac{\eta}{2}\right) \tag{1}$$

where i_0 is the exchange current density, i (current density), F (Faraday constant), R (gas constant), T (absolute temperature), and η (total overpotential) are as defined. As depicted in Figure 3A, the Zn||Zn symmetric cell with the TO-Zn anode has a high exchange current density value (15.1 mA/cm^2), indicating that the TiO_2 interlayer promotes the rapid Zn^{2+} deposition and improves the deposition kinetics [36]. In contrast, the bare Zn anode has a smaller exchange current density value (12.8 mA/cm^2), resulting in an increase in overpotential and slowing the reaction kinetics. As shown in Figure 3B, the curves of the first discharge profiles at 1 mA/cm^2 (1 mA•h/cm^2). During the initial stage of Zn^{2+} deposition, the electrode potential (E) rapidly increases until reaching its maximum value. This stage corresponds to the Zn^{2+} nucleation, where the maximum potential represents the nucleation overpotential (E, ~ 0 V reference in Zn||Zn symmetric cells). The nucleation overpotential of the TO-Zn anode (54.7 mV) is much lower than that of the bare Zn anode (80.9 mV), indicating that the TiO_2 interlayer reduces nucleation overpotential, which is beneficial to the formation of finer Zn nuclei and uniform Zn^{2+} deposition [34, 37].

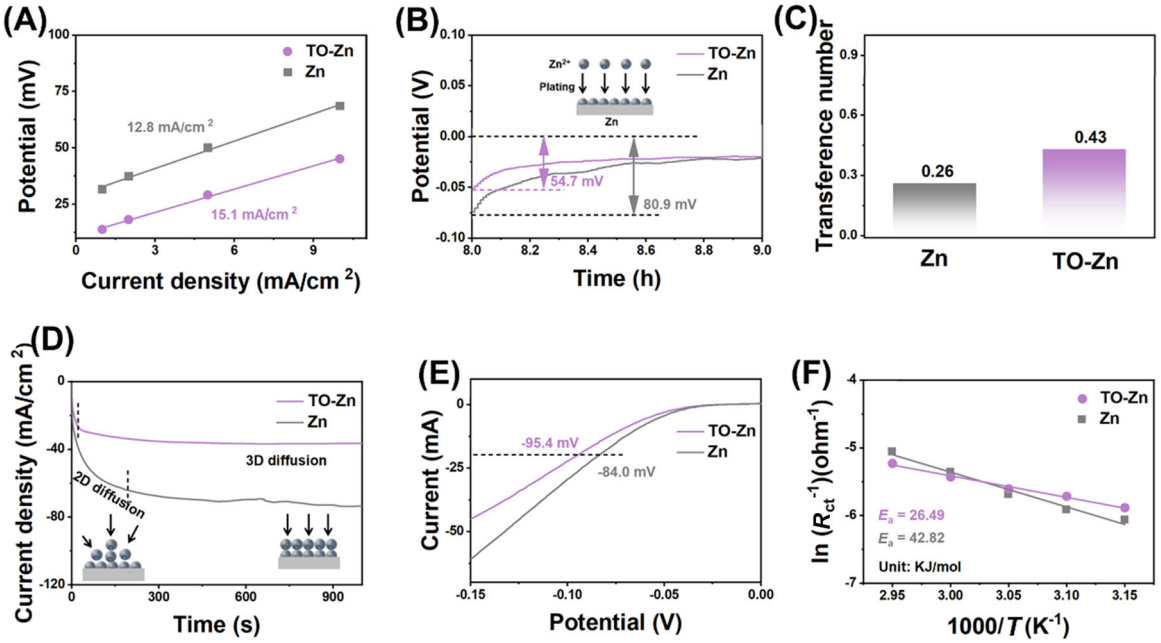

FIGURE 3 | The electrochemical performance of bare Zn and TO-Zn anodes from the Zn||Zn symmetric cells: (A) exchange current density, (B) the first discharge profiles at 1 mA/cm^2 (1 mA•h/cm^2), (C) Zn^{2+} transference numbers ($t_{Zn^{2+}}$), (D) chronoamperometry (CA) curves, (E) LSV curves of different Zn||Ti asymmetric cells, and (F) Arrhenius curves and activation energies of the bare Zn and TO-Zn anodes.

The Zn^{2+} transfer numbers ($t_{Zn^{2+}}$) were obtained from the electrochemical impedance spectroscopy (EIS) and amperometric time–current in Zn | |Zn symmetric cells (Figure S7) [26]. Based on the calculation Equation (2) [38],

$$t_{Zn^{2+}} = \frac{I_s(\Delta V - I_0 R_0)}{I_0(\Delta V - I_s R_s)} \quad (2)$$

where I_0, R_0, I_s, R_s, and ΔV are the initial current, initial resistance, steady-state current, steady-state resistance, and applied voltage polarization, respectively. As shown in Figure 3C, the symmetric cell using the bare Zn anode exhibits a lower $t_{Zn^{2+}}$ (0.26), while the TO-Zn anode provides a high $t_{Zn^{2+}}$ (0.43). Indicating that the TiO_2 interlayer has excellent Zn^{2+} transfer capability, it is beneficial to rapid and uniform Zn^{2+} transfer at the interface, effectively alleviating concentration polarization [39]. In addition, the Zn^{2+} deposition behavior was further studied using chronoamperometry (CA). At a constant overpotential of −150 mV, the bare Zn anode exhibited current density escalation and became unstable in the later stage (Figure 3D). The results indicate that Zn^{2+} undergoes a lengthy 2D diffusion process and tends to accumulate at the tip and form Zn dendrites on the bare Zn anode [40]. In contrast, Zn^{2+} exhibits a continuous three-dimensional (3D) diffusion process after a shorter 2D diffusion period (50 s) on the TO-Zn anode, which facilitates uniform Zn^{2+} deposition. The steady-state current density is lower, indicating a mitigated surface increase resulting from Zn dendrite formation [41].

To evaluate the inhibitory effect of TiO_2 interlayer on side reactions (HER and corrosion), linear sweep voltammetry (LSV) and Tafel were used to test the bare Zn and TO-Zn anodes. As shown in Figure 3E, the LSV test was conducted on Zn||Ti asymmetric cells. At a current of −20 mA, the TO-Zn anode exhibited a reduced voltage (−95.4 mV) compared to the bare Zn anode (−84.0 mV), indicating that the TiO_2 interlayer can inhibit the HER significantly [42]. Calculate the corrosion current density by Tafel curves, as shown in Figure S8. In contrast, the corrosion current density of symmetric cells using TO-Zn anode is lower (0.65 mA/cm^2), indicating that the TiO_2 interlayer can prevent H_2O from corroding the Zn anode [43]. The activation energy (E_a) of bare Zn and TO-Zn anodes was calculated using the Arrhenius Equation (3) [44].

$$\frac{1}{R_{ct}} = Ae^{(-E_a/RT)} \quad (3)$$

where R_{ct} (charge transfer resistance), A (Arrhenius constant), R (gas constant), and T (absolute temperature) are as defined. The E_a of TO-Zn and bare Zn anode obtained from EIS curves tested at various temperatures (45– 65°C) are 26.49 and 42.82 kJ/mol (Figures 3F and S9; Table S1). The lower E_a value indicates that the TiO_2 interlayer promotes the Zn^{2+} desolvation process and effectively improves the redox reaction kinetics at the Zn anode interface [12].

To elucidate the TiO_2 interlayer's role in Zn^{2+} plating/stripping reversibility, the Zn||Cu asymmetric cell was systematically studied at 2 mA/cm^2 (1 mA•h/cm^2). As shown in Figure 4A, the initial coulombic efficiency (ICE) of the bare Zn anode is 95.1%, lower than the TO-Zn anode (96.5%). The lower ICE is mainly due to side reactions hindering the reversibility of the Zn anode, indicating the TiO_2 interlayer can effectively reduce side reactions from the beginning, ensuring the long-term reversibility of the Zn anode [45]. As shown in Figure 4B, the TO-Zn anode maintains a small voltage hysteresis throughout the entire cycling process. Notably, the bare Zn anode shows a large Zn^{2+} plating/stripping voltage gap (59.3 mV), in contrast with the 23.6 mV of the TO-Zn anode (the inset of Figure 4B), which may be due to the TiO_2 interlayer improving the Zn^{2+} diffusion kinetics and reducing concentration polarization [10, 39]. Therefore, the Zn||Cu asymmetric cell with the TO-Zn anode achieves an exceptional average coulomb efficiency (Ave. CE) of 99.9% and a cycle life of over 1300 cycles, indicating that the TiO_2 interlayer plays a critical role in enhancing electrochemical reversibility of the cell (Figure 4C).

The long-term cycling stability evaluation of Zn||Zn symmetric cells with bare Zn and TO-Zn further confirmed that the TiO_2 interlayer can improve cyclic durability. As shown in Figure 4D, the Zn||Zn symmetric cell with TO-Zn anode exhibits symmetric charge–discharge curves and ultra-long cycle life of over 5100 h at 5 mA/cm^2 (1 mA•h/cm^2), which is an approximately 51-fold improvement compared to the bare Zn anode (only 100 h). When a current density of 3 mA/cm^2 (3 mA•h/cm^2), the Zn||Zn symmetrical cells with the TO-Zn anode can still maintain reversible Zn^{2+} plating/stripping for about 1300 h, which is a superior performance compared to the bare Zn anode (Figure S10). In particular, at 10 mA/cm^2 (5 mA•h/cm^2), the cycling life of the TO-Zn anode is close to 450 h (Figure 4E). The TO-Zn anode exhibits significantly enhanced electrochemical performance, with two key advantages: (1) an extended cycling life exceeding 5000 h at 5 mA/cm^2, superior to previously reported artificial interlayer strategies (Figure 4F) [4, 10, 22, 45–50], and (2) markedly reduced voltage hysteresis at 10 mA/cm^2, demonstrating exceptional overpotential stability. This performance improvement is attributed to the synergistic dual functions of TiO_2 interlayer: dendrite-inhibiting physical barrier function and ion-flux homogenization capability, which collectively ensure outstanding electrochemical performance of the battery.

As shown in Figure 5A, the XRD test results indicate that the cathode material used belongs to α-MnO_2. Generally speaking, the α-MnO_2 cathode has a dual platform discharge curve: the first stage (high potential) primarily corresponds to the H^+ insertion mechanism, and the second stage (low potential) corresponds to the co-insertion mechanism of H^+/Zn^{2+} (Figure 5B). The CV curves further indicate that the α-MnO_2 cathode corresponds to the charge storage mechanism of Zn^{2+} and H^+ de-insertion/co-insertion throughout the charging and discharging cycles (Figure 5C) [51]. In addition, the voltage polarization of the CV curve corresponding to the TO-Zn anode is 13 mV lower than that of the bare Zn anode, which can be attributed to the excellent Zn^{2+} transfer ability of the TiO_2 interlayer [15]. As shown in Figure 5D, the midpoint overpotential is 0.25 V (the TO-Zn) and 0.28 V (the bare Zn) at 0.1 A/g, revealing that the TiO_2 interlayer regulates the voltage of the MnO_2 cathode and reduces polarization [39]. In addition, the TO-Zn anode exhibits an initial discharge-specific capacity (262.2 mA•h/g), which is higher than the bare Zn anode

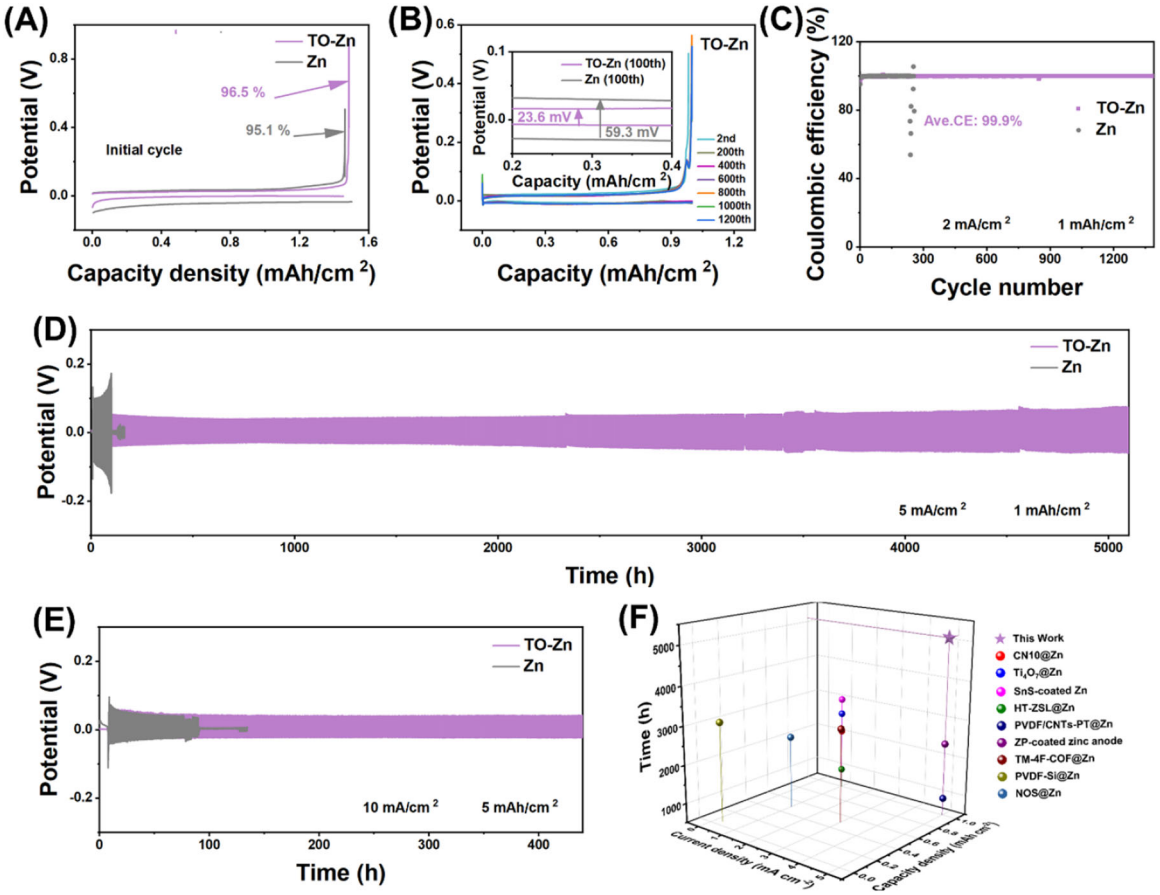

FIGURE 4 | The comparative cycling stability of the bare Zn and TO-Zn anode resulted from electrochemical measurements in Zn||Cu asymmetric and Zn||Zn symmetric cells: (A) the initial voltage capacity profiles, (B) the charge–discharge cycle profiles, and (C) the CE of different Zn||Cu asymmetric cells. The cycling stability of the Zn||Zn symmetric cell using different electrodes at (D) 5 mA/cm^2 (1 mA•h/cm^2) and (E) 10 mA/cm^2 (5 mA•h/cm^2). (F) Comparative cycling performance under varying current densities and capacity densities between this work and the previous ones.

(208.6 mA•h/g). The high discharge-specific capacity of the cathode can be attributed to the reduction of the TO-Zn anode side reactions and the less interference on the electrolyte (the HER effect changes in pH value), so the impact on the cathode is relatively small. As shown in Figure 5E, the influence of the TiO_2 interlayer on charge transfer kinetics was investigated by EIS. In the EIS curve, the semicircle is associated with the charge transfer resistance (R_{ct}), it represents the activation energy barrier for the redox reaction occurring at the electrode interface. The oblique line correlates with the Warburg resistance (R_w), it signifies the diffusion behavior of Zn^{2+}/H^+ in the electrode structure [44]. The result shows that before the first charge–discharge cycle of the Zn||MnO_2 cells, the bare Zn and To-Zn anodes exhibited similar R_{ct} and diffusion impedance. After the first cycle, the TO-Zn anode shows a small ion diffusion resistance, indicating that the TiO_2 interlayer facilitates ion diffusion and improves reaction kinetics at the interface (the inset of Figure 5E). The rate behavior of Zn||MnO_2 full cell with bare Zn and TO-Zn anodes is shown in Figure 5F. At current densities of 0.14, 0.29, 0.71, 1.43, 2.86, and 4.29 A/g, the discharge capacities of the TO-Zn anode are 276.9, 224.2, 172.2, 147.9, 119.8, and 98.2 mA•h/g, respectively. After cycling, the discharge capacity is restored to 282.5 mA•h/g at 0.14 A/g. The rate capability of the TO-Zn anode is better than the bare Zn anode during the entire cycle. The charge–discharge cycle profiles of rate performance in Figure S11 correspond to the de-insertion/co-insertion mechanism of H^+ and Zn^{2+} [51]. As shown in Figure 5G, Zn||MnO_2 full cells assembled with different Zn anodes (with a mass load of approximately 3.8 mg/cm^2) were tested for long-term cycling stability at 1 A/g. The bare Zn||MnO_2 full cell exhibits rapid capacity decay, showing a sharp decline after 640 cycles. In contrast, the full cell assembled with TO-Zn shows a relatively stable cycling performance, retaining a reversible capacity of approximately 108.4 mA•h/g after 1000 cycles, which fully demonstrates the superiority of the TiO_2 interlayer.

3 | Conclusion

In summary, we utilized magnetron sputtering technology to prepare a thin TiO_2 interlayer (approximately 32 nm) on the Zn anode surface (TO-Zn), significantly improving the battery cycling stability. Magnetron sputtering technology has the characteristics of a simple process and high film quality, combined with the stable and uniform nanoscale pore of the TiO_2 interlayer, homogenizing the Zn^{2+} flux and reducing side reactions. The Zn||Zn symmetrical cell with the TO-Zn anode can maintain reversible Zn^{2+} plating/stripping for about 5100 h, and the Zn||Cu asymmetric cell with the TO-Zn anode achieved a high CE of 99.9% and a cycle life of over 1300 cycles. This study presents a feasible and efficient

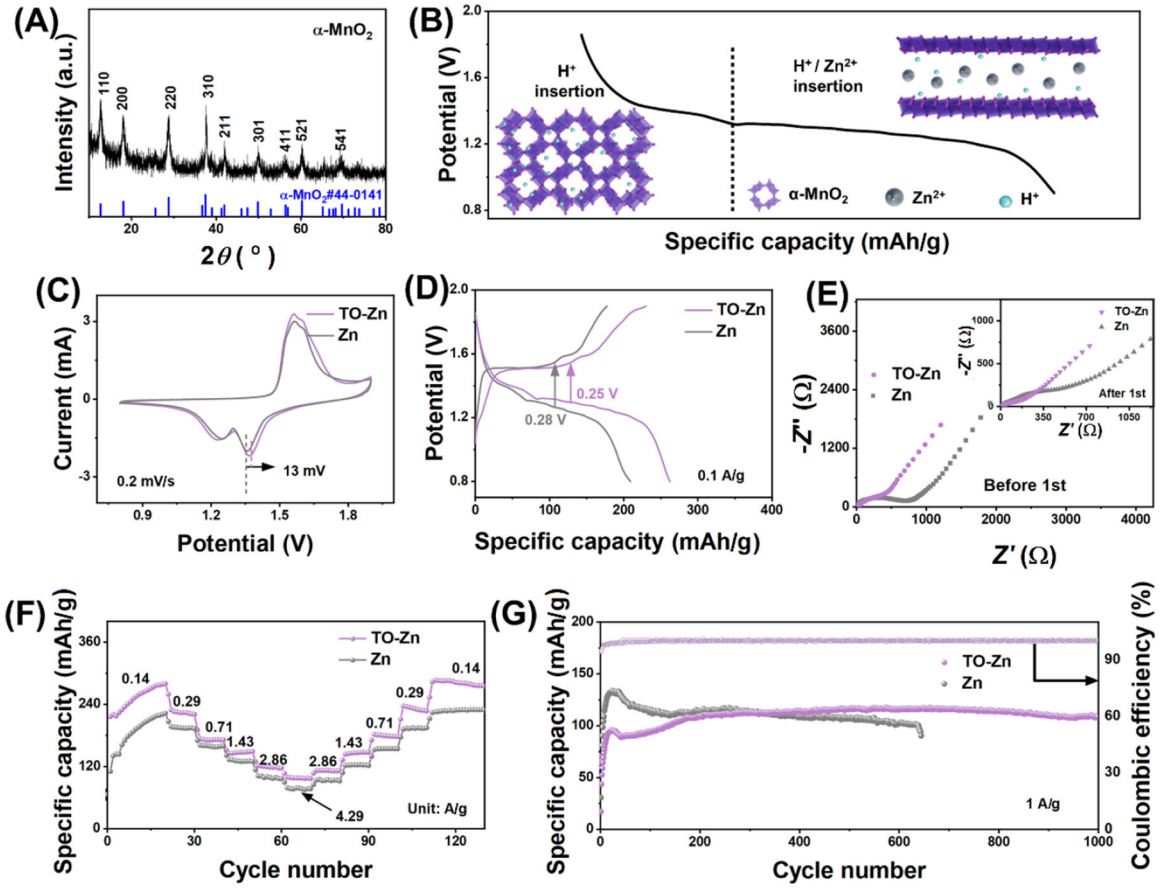

FIGURE 5 | (A) XRD patterns of the α-MnO_2 cathode. (B) Schematic of the reaction mechanism. The electrochemical behavior of bare Zn and TO-Zn anodes resulted from the Zn||MnO_2 full cells: (C) CV curves at 0.2 mV/s, (D) galvanostatic cycling curves at 0.1 A/g, (E) the EIS curves before cycle (the inset is the EIS curves after first cycle), (F) rate performance from 0.14 to 4.29 A/g, and (G) cyclic stabilities and efficiencies at 1 A/g.

design strategy to enhance the cycling stability and lifespan of AZIBs.

Acknowledgments

This work was supported by the National Natural Science Foundation of China (52172044), the Engineering and Physical Sciences Research Council (EP/V027433/1), and the Physical Sciences Research Council (EP/V027433/2). The authors gratefully acknowledge Vastech-Energy and its research team members Sicheng Zheng and Anqi Zhu, for their valuable industrial-oriented contributions to this study.

Conflicts of Interest

The authors declare no conflicts of interest.

Data Availability Statement

The data that support the findings of this study are available from the corresponding author upon reasonable request.

References

1. T. Li, S. Yan, H. Dong, et al., "Engineering Hydrophobic Protective Layers on Zinc Anodes for Enhanced Performance in Aqueous Zinc-Ion Batteries," *Journal of Energy Chemistry* 97 (2024): 1–11.

2. Z. Liu, R. Wang, Y. Gao, et al., "Low-Cost Multi-Function Electrolyte Additive Enabling Highly Stable Interfacial Chemical Environment for Highly Reversible Aqueous Zinc Ion Batteries," *Advanced Functional Materials* 33, no. 49 (2023): 2308463.

3. R. Zhao, Y. Yang, G. Liu, et al., "Redirected Zn Electrodeposition by an Anti-Corrosion Elastic Constraint for Highly Reversible Zn Anodes," *Advanced Functional Materials* 31, no. 2 (2021): 2001867.

4. J. Wang, J. Peng, W. Huang, et al., "Enabling Stable Zn Anode With PVDF/CNTs Nanocomposites Protective Layer Toward High-Performance Aqueous Zinc-Ion Batteries," *Advanced Functional Materials* 34, no. 26 (2024): 2316083.

5. X. Xiao, X. Ye, Z. Wu, et al., "Trace Small Molecular/Nano-Colloidal Multiscale Electrolyte Additives Enable Ultra-Long Lifespan of Zinc Metal Anodes," *Advanced Materials* 36, no. 38 (2024): 2408706.

6. D. Wang, H. Liu, D. Lv, C. Wang, J. Yang, and Y. Qian, "Rational Screening of Artificial Solid Electrolyte Interphases on Zn for Ultrahigh-Rate and Long-Life Aqueous Batteries," *Advanced Materials* 35, no. 2 (2023): 2207908.

7. X. Sun, X. Lv, M. Zhang, et al., "Construction of Selective Ion Transport Polymer at Anode–Electrolyte Interface for Stable Aqueous Zinc-Ion Batteries," *ACS Nano* 18, no. 11 (2024): 8452–8462.

8. N. Guo, Z. Peng, W. Huo, et al., "Stabilizing Zn Metal Anode Through Regulation of Zn Ion Transfer and Interfacial Behavior With a Fast Ion Conductor Protective Layer," *Small* 19, no. 47 (2023): 2303963.

9. R. Zhang, Y. Feng, Y. Ni, et al., "Bifunctional Interphase With Target-Distributed Desolvation Sites and Directionally Depositional Ion Flux for Sustainable Zinc Anode," *Angewandte Chemie International Edition* 62, no. 25 (2023): e202304503.

10. Y. Song, Y. Liu, S. Luo, et al., "Blocking the Dendrite-Growth of Zn Anode by Constructing Ti_4O_7 Interfacial Layer in Aqueous Zinc-Ion Batteries," *Advanced Functional Materials* 34, no. 25 (2024): 2316070.

11. H. Wang, P. Wang, K. Yu, et al., "Constructing a Rapid Ion-Transport Anode Interface Protective Layer for Zinc Ion Batteries to Suppress Solvation and Improve Surface Electronic Structure," *Chemical Engineering Journal* 485 (2024): 149544.

12. X. Yang, C. Li, Z. Sun, et al., "Interfacial Manipulation via in Situ Grown ZnSe Cultivator Toward Highly Reversible Zn Metal Anodes," *Advanced Materials* 33, no. 52 (2021): 2105951.

13. S. Zhang, M. Ye, Y. Zhang, Y. Tang, X. Liu, and C. C. Li, "Regulation of Ionic Distribution and Desolvation Activation Energy Enabled by In Situ Zinc Phosphate Protective Layer Toward Highly Reversible Zinc Metal Anodes," *Advanced Functional Materials* 33, no. 22 (2023): 2208230.

14. J. Hao, B. Li, X. Li, et al., "An In-Depth Study of Zn Metal Surface Chemistry for Advanced Aqueous Zn-Ion Batteries," *Advanced Materials* 32, no. 34 (2020): 2003021.

15. Y. Liu, T. Guo, Q. Liu, et al., "Ultrathin ZrO_2 Coating Layer Regulates Zn Deposition and Raises Long-Life Performance of Aqueous Zn Batteries," *Materials Today Energy* 28 (2022): 101056.

16. J. Yang, R. Zhao, Y. Wang, et al., "Insights on Artificial Interphases of Zn and Electrolyte: Protection Mechanisms, Constructing Techniques, Applicability, and Prospective," *Advanced Functional Materials* 33, no. 14 (2023): 2213510.

17. D. Chaussende, V. Tabouret, A. Crisci, et al., "Investigation of Amorphous-SIC Thin Film Deposition by RF Magnetron Sputtering for Optical Applications," *Materials Science in Semiconductor Processing* 182 (2024): 108673.

18. M. Gholami, K. Khojier, M. Monsefi, and S. M. Borghei, "Fabrication and Characterization of Ta_xN Thin Films Deposited by DC Magnetron Sputtering Technique: Application in Microelectronic Devices," *Brazilian Journal of Physics* 52, no. 5 (2022): 171.

19. Y. Pan, J. Wang, Z. Lu, R. Wang, and Z. Xu, "A Review on the Application of Magnetron Sputtering Technologies for Solid Oxide Fuel Cell in Reduction of the Operating Temperature," *International Journal of Hydrogen Energy* 50 (2024): 1179–1193.

20. H. Skliarova, S. Cisternino, E. Cazzola, et al., "PP#83-Use of Magnetron Sputtering Technique for Medical Cyclotron Solid Target Preparation," *Nuclear Medicine and Biology* 72 (2019): S31.

21. S. Yan, X. Yan, Y. Tong, M. Zhang, and J. Liu, "Application of Magnetron Sputtering Technique to Fabricate Sulfur/Carbon Composites Cathode Plates of Lithium-Sulfur Battery," *Materials Letters* 273 (2020): 127888.

22. F. Zhao, J. Feng, H. Dong, et al., "Ultrathin Protection Layer via Rapid Sputtering Strategy for Stable Aqueous Zinc Ion Batteries," *Advanced Functional Materials* 34, no. 51 (2024): 2409400.

23. Q. Zhang, J. Luan, X. Huang, et al., "Revealing the Role of Crystal Orientation of Protective Layers for Stable Zinc Anode," *Nature Communications* 11, no. 1 (2020): 3961.

24. Y. Zhu, G. Liang, X. Cui, et al., "Engineering Hosts for Zn Anodes in Aqueous Zn-Ion Batteries," *Energy & Environmental Science* 17, no. 2 (2024): 369–385.

25. J. Zheng, Z. Huang, Y. Zeng, et al., "Electrostatic Shielding Regulation of Magnetron Sputtered Al-Based Alloy Protective Coatings Enables Highly Reversible Zinc Anodes," *Nano Letters* 22, no. 3 (2022): 1017–1023.

26. L. Hong, X. Wu, L.-Y. Wang, et al., "Highly Reversible Zinc Anode Enabled by a Cation-Exchange Coating With Zn-Ion Selective Channels," *ACS Nano* 16, no. 4 (2022): 6906–6915.

27. T. Wang, P. Wang, L. Pan, et al., "Stabling Zinc Metal Anode With Polydopamine Regulation Through Dual Effects of Fast Desolvation and Ion Confinement," *Advanced Energy Materials* 13, no. 5 (2023): 2203523.

28. M. Zhou, S. Guo, J. Li, et al., "Surface-Preferred Crystal Plane for a Stable and Reversible Zinc Anode," *Advanced Materials* 33, no. 21 (2021): 2100187.

29. K. S. Sánchez-Zambrano, M. Hernández-Reséndiz, C. Gómez-Rodríguez, et al., "XPS Study on Calcining Mixtures of Brucite With Titania," *Materials* 15, no. 9 (2022): 3117.

30. J. Yang, Y. Zhang, K. Liu, et al., "Z-Scheme Heterojunction of Phosphorus-Doped Carbon Nitride/Titanium Dioxide: Photocatalytic Performance," *Molecules* 29, no. 18 (2024): 4342.

31. Z. Guo, L. Fan, C. Zhao, et al., "A Dynamic and Self-Adapting Interface Coating for Stable Zn-Metal Anodes," *Advanced Materials* 34, no. 2 (2022): 2105133.

32. T. Sudare, R. Shimizu, N. Yamada, et al., "Elucidating the Role of Interstitial Oxygen in Transparent Conducting Anatase TiO_2 by Polarized X-Ray Absorption Spectroscopy Study," *Chemistry of Materials* 37, no. 1 (2025): 480–488.

33. Y. Cui, Z. Ju, R. Yu, et al., "Challenges, Strategies, and Perspectives of Anode Protection in Aqueous Zinc-Ion Batteries," *ACS Materials Letters* 6, no. 2 (2024): 611–626.

34. X. Yu, Z. Li, X. Wu, et al., "Ten Concerns of Zn Metal Anode for Rechargeable Aqueous Zinc Batteries," *Joule* 7, no. 6 (2023): 1145–1175.

35. Y. Dai, C. Zhang, W. Zhang, et al., "Reversible Zn Metal Anodes Enabled by Trace Amounts of Underpotential Deposition Initiators," *Angewandte Chemie International Edition* 62, no. 18 (2023): e202301192.

36. J. Zhou, F. Wu, Y. Mei, et al., "Establishing Thermal Infusion Method for Stable Zinc Metal Anodes in Aqueous Zinc-Ion Batteries," *Advanced Materials* 34, no. 21 (2022): 2200782.

37. Y. Song, P. Ruan, C. Mao, et al., "Metal–Organic Frameworks Functionalized Separators for Robust Aqueous Zinc-Ion Batteries," *Nano-Micro Letters* 14, no. 1 (2022): 218.

38. W. Zhang, X. Zhu, L. Kang, et al., "Stabilizing Zinc Anode Using Zeolite Imidazole Framework Functionalized Separator for Durable Aqueous Zinc-Ion Batteries," *Journal of Energy Chemistry* 90 (2024): 23–31.

39. H. Liu, Q. Ye, D. Lei, et al., "Molecular Brush: An Ion-Redistributor to Homogenize Fast Zn^{2+} Flux and Deposition for Calendar-Life Zn Batteries," *Energy & Environmental Science* 16, no. 4 (2023): 1610–1619.

40. T. Shen, M. Fang, T. Lv, et al., "In Situ Assembly of Metal-Organic Coordination Polymer Layers Enables Highly Reversible Zn Anodes With a Long Cycle Life of Over 6900 h," *Advanced Functional Materials* 34, no. 48 (2024): 2408578.

41. Z. Zhao, J. Zhao, Z. Hu, et al., "Long-Life and Deeply Rechargeable Aqueous Zn Anodes Enabled by a Multifunctional Brightener-Inspired Interphase," *Energy & Environmental Science* 12, no. 6 (2019): 1938–1949.

42. Y. Ai, C. Yang, Z. Yin, et al., "Biomimetic Superstructured Interphase for Aqueous Zinc-Ion Batteries," *Journal of the American Chemical Society* 146, no. 22 (2024): 15496–15505.

43. B. -b. Sui, L. Sha, P. -f. Wang, et al., "In Situ Zinc Citrate on the Surface of Zn Anode Improves the Performance of Aqueous Zinc-Ion Batteries," *Journal of Energy Storage* 82 (2024): 110550.

44. H. Qiu, X. Du, J. Zhao, et al., "Zinc Anode-Compatible In-Situ Solid Electrolyte Interphase via Cation Solvation Modulation," *Nature Communications* 10, no. 1 (2019): 5374.

45. J. H. Park, C. Choi, J. B. Park, S. Yu, and D.-W. Kim, "Fortifying Zinc Metal Anodes Against Uncontrollable Side-Reactions and Dendrite Growth for Practical Aqueous Zinc Ion Batteries: A Novel Composition of Anti-Corrosive and Zn^{2+} Regulating Artificial Protective Layer," *Advanced Energy Materials* 14, no. 5 (2024): 2302493.

46. Y. Wang, N. Li, H. Liu, et al., "Interface Regulation Using a Fluorinated Vinylene-Linked Covalent Organic Framework for a Highly Stable Zn Anode," *Journal of Materials Chemistry A* 12, no. 13 (2024): 7799–7806.

47. C.-Y. Tian, W.-W. Li, X.-W. Liu, et al., "Hydrophobic Organic–Inorganic Hybrid Surface Modification-Induced Uniform Zinc Deposition and Prohibited Side Reactions Toward a Ultra-Stable Zinc Anode," *ACS Sustainable Chemistry & Engineering* 11, no. 9 (2023): 3576–3584.

48. H. J. Kim, S. Kim, K. Heo, J. Lim, H. Yashiro, and S. Myung, "Nature of Zinc-Derived Dendrite and Its Suppression in Mildly Acidic Aqueous Zinc-Ion Battery," *Advanced Energy Materials* 13, no. 2 (2023): 2203189.

49. Y. Hu, C. Fu, S. Chai, et al., "Construction of Zinc Metal-Tin Sulfide Polarized Interface for Stable Zn Metal Batteries," *Advanced Powder Materials* 2, no. 2 (2023): 100093.

50. H. Zhang, T. Jiang, D. Jin, L. Xie, and M. Wu, "Hydrophobic and Zincophilic Organic Hierarchical Nano-Membranes With Ordered Molecular Packing for Stable Zinc Metal Anodes," *Energy Storage Materials* 70 (2024): 103513.

51. J. Huang, Z. Wang, M. Hou, et al., "Polyaniline-Intercalated Manganese Dioxide Nanolayers as a High-Performance Cathode Material for an Aqueous Zinc-Ion Battery," *Nature Communications* 9, no. 1 (2018): 2906.

Supporting Information

Additional supporting information can be found online in the Supporting Information section.

Figure S1: SEM images of (A) bare Zn anode and (B) TO-Zn anode. **Figure S2:** (A, B) Structure of Zn atoms on bare Zn anode and TO-Zn anode surfaces, (C) the binding energies of Zn atoms onto bare Zn anode and TO-Zn anode surfaces. (D) calculated structure model of Zn (101). (E, F) Crystal structure of TiO_2 (101), and calculated structure model of amorphous TiO_2 interlayer. **Figure S3:** The AFM image was taken at the step edge of the TiO_2 interlayer on a Zn surface. **Figure S4:** The EDS images of the bare Zn anode resulted from the Zn||Zn symmetric cell after 10 cycles at 1 mA/cm^2 for 1 $mA{\cdot}h/cm^2$. **Figure S5:** (A, B) The SEM images of the bare Zn and TO-Zn anodes resulted from the symmetric cells after 1 cycle at 10 mA/cm^2 for 10 $mA{\cdot}h/cm^2$. **Figure S6:** The rate performances of the Zn||Zn symmetric cells at different current densities with a fixed capacity of 1 $mA{\cdot}h/cm^2$. **Figure S7:** (A, B) Current density-time curves of different Zn||Zn symmetric cells during the polarization tests. Insets in (A) and (B) are EIS curves of the corresponding cells before and after polarization. **Figure S8:** Tafel curves of the bare Zn and TO-Zn anodes resulted from the Zn||Zn symmetric cells. **Figure S9:** (A, B) EIS curves of different Zn||Zn symmetric cells at different temperatures. **Figure S10:** Cycling performance of Zn||Zn symmetric cells using different electrodes at 3 mA/cm^2 for 3 $mA{\cdot}h/cm^2$. **Figure S11:** (A, B) Charge-discharge cycle profiles of rate performance using TO-Zn and bare Zn anodes. **Table S1:** The charge-transfer resistance values (R_{ct}) of Zn||Zn symmetric cells assembled using bare Zn and TO-Zn at different temperatures.